DOUBLY IMAGED QUASAR SDSS J1515+1511: TIME DELAY AND LENSING GALAXIES

Vyacheslav N. Shalyapin[1,2] and Luis J. Goicoechea[2]

[1]Institute for Radiophysics and Electronics, National Academy of Sciences of Ukraine, 12 Proskura St., 61085 Kharkov, Ukraine; vshal@ukr.net

[2]Departamento de Física Moderna, Universidad de Cantabria, Avda. de Los Castros s/n, 39005 Santander, Spain; goicol@unican.es

ABSTRACT

We analyse new optical observations of the gravitational lens system SDSS J1515+1511. These include a 2.6–year photometric monitoring with the Liverpool Telescope (LT) in the r band, as well as a spectroscopic follow–up with the LT and the Gran Telescopio Canarias (GTC). Our r–band LT light curves cover a quiescent microlensing period of the doubly imaged quasar at $z_{\rm s} = 2.049$, which permits us to robustly estimate the time delay between the two images A and B: 211 ± 5 days (1σ confidence interval; A is leading). Unfortunately, the main lensing galaxy (G1) is so faint and close to the bright quasar that it is not feasible to accurately extract its spectrum through the GTC data. However, assuming the putative redshift $z_{\rm G1} = 0.742$, the GTC and LT spectra of the distant quasar are used to discuss the macrolens magnification, and the extinction and microlensing effects in G1. The new constraints on the time delay and macrolens magnification ratio essentially do not change previous findings on the mass scale of G1 and external shear, while the redshift of the lensing mass is found to be consistent with the assumed value of $z_{\rm G1}$. This is a clear evidence that G1 is indeed located at $z_{\rm G1} = 0.742$. From the GTC data we also obtain the redshift of two additional objects (the secondary galaxy G2 and a new absorption system) and discuss their possible role in the lens scenario.

Keywords: gravitational lensing: strong — quasars: individual (SDSS J1515+1511)

1. INTRODUCTION

Optical light curves and spectra of gravitationally lensed quasars show different phases of microlensing activity induced by stars in lensing galaxies, and each of these phases is relevant for certain astrophysical studies. Periods of high microlensing activity were reported for several systems, including prominent flux variations (e.g., Udalski et al. 2006; Hainline et al. 2013), significant spectral distortions (e.g., Richards et al. 2004; Rojas et al. 2014), or both (e.g., Goicoechea & Shalyapin 2016). Such high activity is related to stellar mass microlenses strongly affecting the accretion disk and the innermost part of the broad line region (BLR), while the narrow line region (NLR) remains unaffected (e.g., Schneider & Wambsganss 1990; Abajas et al. 2002). Hence, a strong microlensing episode in a lensed quasar can be used to probe the structure of its accretion disk and BLR, as well as the composition of the main lensing galaxy (e.g., Mosquera & Kochanek 2011, and references therein). Unfortunately, when an important extrinsic (microlensing) variability is present in the light curve of an image of a lensed quasar, it is difficult to accurately measure the time delay between that image and any other. Only in some cases, time delays were measured to $\sim 5\%$ precision after monitoring during $5-10$ year periods and using sophisticated techniques of analysis (e.g., Ofek & Maoz 2003; Morgan et al. 2008; Hainline et al. 2013).

Time delays can be used to constrain the Hubble constant (and other cosmological parameters) and lensing mass distributions (e.g., Refsdal 1964, 1966; Schneider et al. 2006). Therefore, lensed quasars with two or more images in quiescent phases of microlensing activity are ideal targets to determine delays and study the Universe on different scales. Knowing the time delay between two quiescent images of the same quasar, if we detect a sharp variation in the optical flux of the leading image, a multiwavelength campaign can be planned to follow the variability of the trailing one. Multiwavelength intrinsic variations in this trailing image are valuable tools to carry out reverberation mapping studies (e.g., Gil-Merino et al. 2012; Dahle et al. 2015), and thus check the quasar structure derived from active microlensing periods. Time delays from quiescent images and images showing smooth microlensing variations are often measured to $\leq 3\%$ precision (e.g., Eulaers et al. 2013; Rathna Kumar et al. 2013), and sometimes to precision levels as low as a few tenths of a percent (e.g., Kundić et al. 1997; Shalyapin et al. 2008).

The lensed quasar SDSS J1515+1511 consists of two optically bright images (A and B) separated by $\sim 2''$ (Inada et al. 2014). Although Inada et al. reported a source redshift $z_{\rm s} = 2.054$, this relies on the SDSS spectrum of the A image taken in 2007, which has all its emission features at $z_{\rm em} = 2.049$. It is also worth to note that the SDSS/BOSS spectrum of A in 2012, as well as the new spectra of A and B in 2015 (see Section 2.2.1), contain emission lines at a redshift of 2.049. We thus adopt $z_{\rm s} = z_{\rm em} = 2.049$ throughout this paper. Inada et al. also presented spectra of A and B that were obtained through a 900 s exposure with the DOLORES spectrograph on the 3.6 m Telescopio Nazionale Galileo (TNG). They found strong Mg II absorption at $\sim$4900 Å in the spectrum of B (the image closer to the main lensing galaxy G1). Such an absorption feature corresponds to intervening gas at a redshift of 0.742, suggesting that $z_{\rm G1} = 0.742$. New Subaru Telescope adaptive–optics observations in the K'–band improved the relative astrometry of the lens system and the morphological parameters of G1 (Rusu et al. 2016). Rusu et al. also detected a secondary galaxy G2 southwest of the ABG1 system and predicted the time delay $\Delta t_{\rm AB}$ for three different lens models. To perform this model fitting, the macrolens magnification ratio $\Delta m_{\rm AB}$ was constrained within an interval based on the K'–band magnitude difference $B - A$. The expected value of $\Delta t_{\rm AB}$ ranged from ~ 145 to ~ 216 days, with the longest delay for the most realistic model: singular isothermal ellipsoid plus external shear (SIE+γ).

Here we focus on observations of SDSS J1515+1511 during a quiescent phase of microlensing activity over the 2014−2016 period. The outline of the paper is the following: Section 2 presents a 2.6–year photometric monitoring of both quasar images, and spectroscopic follow–up observations of the lens system. These last observations include new long–slit spectra that are 50 times deeper than the previous ones with the TNG (see above). Section 3 is devoted to accurately measure $\Delta t_{\rm AB}$, while we estimate $\Delta m_{\rm AB}$ in Section 4. In Section 4, we also discuss the dust extinction and microlensing magnification in G1. In Section 5, we update the SIE+γ lens model, confirm the tentative redshift of G1, and discuss the role of G2 (and other intervening object) in the lensing phenomenon. Our main results and conclusions appear in Section 6.

2. OBSERVATIONS AND DATA REDUCTION

2.1. *Photometric monitoring*

We conducted a photometric monitoring campaign of SDSS J1515+1511 from early February of 2014 to mid September of 2016, i.e., for 2.6 years with an average sampling rate of about two nights every week. All optical observations were performed with the 2.0 m fully robotic Liverpool Telescope (LT) at the Roque de los Muchachos Observatory, Canary Islands (Spain), using the IO:O CCD camera (pixel scale of $0''.30$). Each observing night, 2×300 s exposures were taken in the r Sloan passband, and the corresponding frames were subsequently passed through a pre–processing pipeline. The LT data reduction pipeline included bias subtraction, overscan trimming, and flat fielding. In addition, we cleaned cosmic rays and interpolated over bad pixels using the bad pixel mask[1].

After the basic reduction of frames, we assumed that the point–spread function (PSF) for each exposure is defined by the surface brightness distribution of the unsaturated star with $r = 16.770$ mag in the vicinity of the lens system (see the left panel of Figure 1). We also adopted this PSF star as the reference object for differential photometry. The relative fluxes and magnitudes of both quasar images were then derived through PSF fitting. Our crowded–field photometry pipeline relied on IRAF[2] tasks and the IMFITFITS software (McLeod et al. 1998), while the photometric model consisted of two PSFs (A and B), an exponential profile convolved with the PSF (G1 galaxy located between A and B), and a constant background. Inada et al. (2014) reported that the Sérsic index of G1 is consistent with $n = 1$ (exponential profile), instead of $n = 4$ (de Vaucouleurs profile). Moreover, Rusu et al. (2016) found that G1 is an edge–on disk–like galaxy. The ellipticity, orientation, and effective radius of G1, as well as the relative positions of B and G1 (with respect to A), were taken from Rusu et al. (2016).

The galaxy brightness was estimated from the best frames in terms of signal–to–noise ratio (SNR) and full–width at half–maximum (FWHM) of the seeing disc. These frames led to a galaxy–to–PSF star ratio $G1/PSF = 0.005$, or equivalently, $r(G1) = 22.5$ mag. We then applied our pipeline to the 310 usable frames, incorporating this $G1/PSF$ value as additional constraint. As G1 is very faint in the r band, and the magnitude difference between G1 and the faintest quasar image is $\sim$4 ($B/G1 \sim 40$), we note that the adopted galaxy model does not play a critical role in extracting quasar fluxes. We identified 19 frames producing outliers in the quasar light curves, so these were removed from the final database. The remaining 291 frames (average FWHM of $\sim 1''.4$) allowed us to obtain r–SDSS magnitudes

---

[1] The pre–processed frames will be soon publicly available on the GLENDAMA archive at http://grupos.unican.es/glendama/database/ (Goicoechea et al. 2015).

[2] IRAF is distributed by the National Optical Astronomy Observatory, which is operated by the Association of Universities for Research in Astronomy (AURA) under cooperative agreement with the National Science Foundation. This software is available at http://iraf.noao.edu/.

of A and B at 150 nights (epochs). We also calculated the magnitudes of a field star at these epochs. The field star has a brightness similar to that of A, and is located between the lens system and the PSF star (see the left panel of Figure 1).
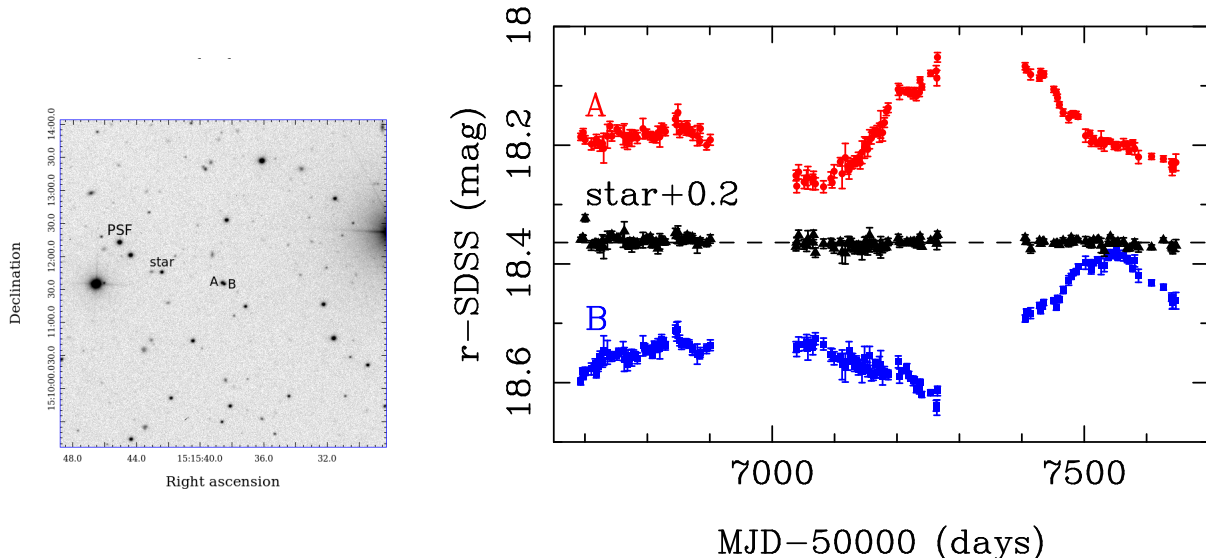
Figure 1. Left: First LT frame of SDSS J1515+1511 on 2014 February 4. This 300 s exposure in the r band was taken under typical seeing conditions (FWHM = 1″3), just a few weeks after the announcement of the discovery by N. Inada and coworkers. The field of view covers $5' \times 5'$, and includes the blended quasar images (A and B), the PSF star, and a field star that lies about midway between the lensed quasar and the PSF star. Right: LT r–band light curves of A, B and the field star. The stellar curve is shifted by +0.2 mag to facilitate comparison.

Table 1. LT r–band light curves of SDSS J1515+1511AB.

MJD–50000	A[a]	σ_A[a]	B[a]	σ_B[a]	S[ab]	σ_S[ab]
6693.260	18.186	0.006	18.598	0.006	18.159	0.004
6696.282	18.183	0.007	18.582	0.007	18.156	0.005
6697.263	18.179	0.007	18.588	0.007	18.157	0.005
6700.232	18.191	0.007	18.581	0.007	18.123	0.006
6710.173	18.198	0.010	18.577	0.010	18.169	0.008

[a] r–SDSS magnitude.

[b] We use S to denote the field (control) star.

NOTE—Table 1 is published in its entirety in the machine-readable format. A portion is shown here for guidance regarding its form and content.

To estimate typical photometric errors in the light curves of A, B, and the star, we first determined the standard deviations between magnitudes having time separations < 2.5 days, and then such deviations were divided by the square root of 2 (e.g., Goicoechea & Shalyapin 2010). This procedure led to a typical uncertainty of 0.0085 mag in the brightness of both quasar images, which is slightly larger than the typical error in the star (0.0065 mag). We also considered that $\sigma_r \propto 1/\mathrm{SNR}$ (e.g., Howell 2006) to infer nightly errors in the light curves. Table 1 includes the final r–SDSS magnitudes and errors for A, B and the star. These brightness records are also shown in the right panel of Figure 1. Apart from the two unavoidable seasonal gaps, the quasar variability is accurately traced.

2.2. Spectroscopic follow–up

2.2.1. Deep long–slit spectra

Deep long–slit spectra of SDSS J1515+1511 were obtained using the R500B and R500R grisms in the OSIRIS spectrograph on the 10.4 m Gran Telescopio Canarias (GTC)[3]. The slit was oriented along the line joining both quasar images, and its width was $1''23$ (~ 5 pixel). We took a single 1800 s exposure with the blue grism (R500B) on 2015 April 15 under good observing conditions: dark and photometric night, FWHM $= 0''95$ at the central wavelength $\lambda_c = 4745$ Å, and airmass of 1.04. We also observed the lens system with the red grism (R500R) on 2015 April 16. This second grey night, 3×1800 s exposures were taken under variable seeing (FWHM $= 1''19$, $0''89$, and $0''79$ at λ_c $= 7165$ Å) and airmass (1.04, 1.06, and 1.10). Hence, the new data cover a wavelength range of $3570-9250$ Å with a resolving power of $\sim 300-400$. Observations of the spectrophotometric standard star Ross 640 (Oke 1974) were performed with a wider slit of $2''52$, which forced us to carry out a careful flux calibration from photometric data (see below).

For each grism, through a standard data reduction with IRAF, we obtained a sky–subtracted, wavelength–calibrated spectrum for each ~ 5 pixel slice along the slit. However, the extraction of the individual spectra of A, B, and G1 is not a simple task. We deal with three sources next to each other. Moreover, there is high brightness contrast between B and G1 (e.g., $B/G1 \sim 40$ in the r band), only $0''4$ apart. These complications prevented detection of G1 using the blue grism data. Among the known extraction techniques (e.g., Fassnacht & Cohen 1998; Ofek et al. 2006; Sluse et al. 2007; Shalyapin & Goicoechea 2014), after some tests, we chose a method similar to that of Sluse et al. (2007). They derived spectra for three close point–like sources along a slit by fitting three 1D Moffat profiles for each wavelength bin. Although G1 is an extended source, it has a very large ellipticity with position angle almost perpendicular to the slit axis, and its effective radius in the spatial direction is $\sim 0''13$ (Rusu et al. 2016). Thus, in the spatial direction, this very faint galaxy can be treated as a point–like object (we checked the validity of this approach). For the red grism, our initial model consisted of three 1D Moffat profiles (A+B+G1) at each wavelength, while we only considered two components (A+B) when analysing the blue grism data.
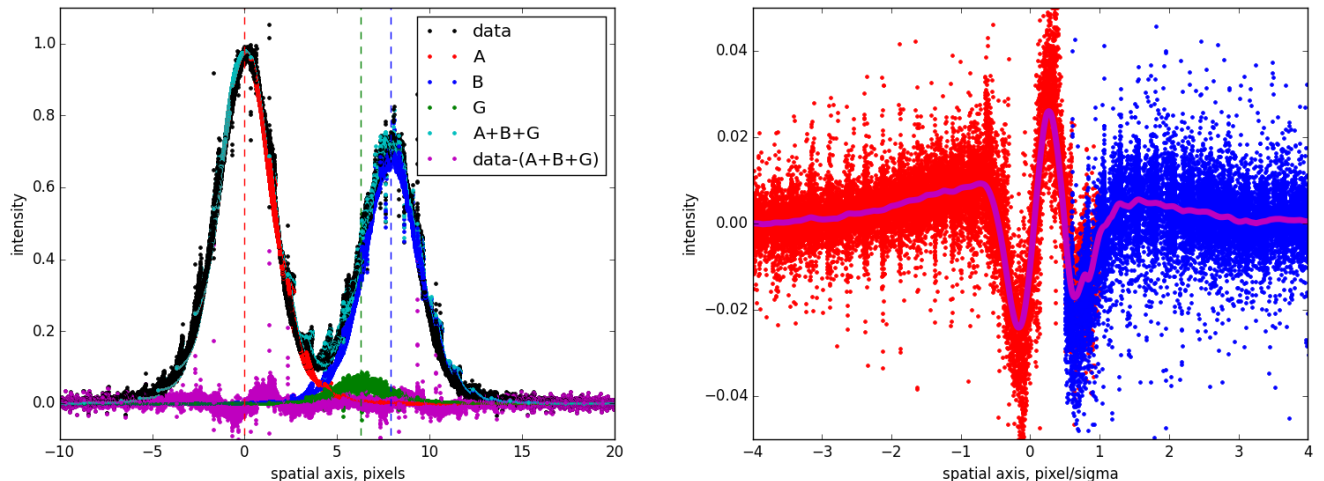
Figure 2. GTC–OSIRIS–R500R fluxes along the slit. Left: Normalized spatial profile as a result of combining the 1D flux distributions for all wavelength bins. The measured fluxes (data) are compared with fitted fluxes, using a model that consists of three 1D Moffat profiles (A+B+G1) at each wavelength. Right: Differences between the true PSF and the Moffat function. These residuals (PSF − Moffat) come from the central region and the left wing of A (red circles), and the right wing of B (blue circles). The smoothed behaviour (purple line) is the LUT correction (see main text).

From now on, we are going to describe in detail the extraction of the individual spectra of A, B, and G1, via the red grism data. We used the Rusu et al.'s astrometry to set the positions of B and G1 with respect to A. In addition, the 1D Moffat function is characterized by three parameters: centroid, slope, and width, and after preliminary data analysis, we also fixed a global value (the same at all wavelengths) for the slope (Jahnke et al. 2007). Thus, in a

---

[3] The OSIRIS User Manual (v3.1) by A. Cabrera-Lavers is available at http://www.gtc.iac.es/instruments/osiris.

first iteration, only the position (centroid) of A, the width of the Moffat function, and the amplitudes of the three components were allowed to vary at each wavelength. The first fits to the multi–wavelength 1D flux distributions generated wavelength–dependent values of the position of A and the width of the 1D PSF model, which were fitted to smooth polynomial functions. In a second iteration, these two position–structure parameters were evaluated by their polynomial laws, leaving only the amplitudes as free parameters. We then obtained the fluxes of A, B, and G1 through the fitted amplitudes and the observational priors for the structure parameters of the PSF model.

Although the second iteration produces accurate spectra of the quasar images, the spectrum of G1 is not as smooth as would be desired. The PSF shape is not perfectly described with a Moffat function, and residuals (data − model) are comparable to the 1D fluxes of G1. Because of the existence of this important residuals–induced noise, we refined the PSF model to try to remove/minimize residuals with an empirical look–up–table (LUT) correction (e.g., Møller 2000; Jahnke et al. 2007). Following Møller (2000), the ∼1000 measured spatial profiles (1D flux distributions) were combined into the single normalized distribution that is shown in the left panel of Figure 2. The differences between measured and fitted fluxes (purple circles) display a regular spatial pattern, and we focused on a region around and to the left of the centroid of A, as well as on a region to the right of the centroid of B. Both regions basically include the residuals of interest, i.e., differences between the true PSF and the Moffat function. In the right panel of Figure 2, we present properly scaled residuals for a PSF centered at $x = 0$. These were smoothed in order to reduce noise (see the purple line in the right panel of Figure 2), and then incorporated into a refined PSF model: analytical Moffat function plus empirical LUT.

In a third iteration, we used Moffat+LUT profiles to describe the contributions of the three sources (quasar images and main lensing galaxy) at each wavelength, and thus obtained the final instrumental spectra of A, B, and G1. From the instrumental spectrum of the standard star, we also built the spectral response function, and corrected the instrumental fluxes of the quasar and the galaxy. Unfortunately, the standard star was observed with a relatively wide slit (see above), which did not allow us to accurately calibrate the flux scale. In order to calibrate the quasar spectra, we used r–band fluxes of A and B from LT frames taken on 2015 April 16 (see Section 2.1). To fix the flux scale of G1, we also considered the i–band flux of the galaxy by Inada et al. (2014). Our final flux–calibrated spectra of the lens system (blue and red grisms) are shown in Figure 3. Tables 2 and 3 include the spectra of the lens system from the blue and red grism data, respectively. Additionally, all raw and reduced frames in FITS format are publicly available at the GTC archive[4].

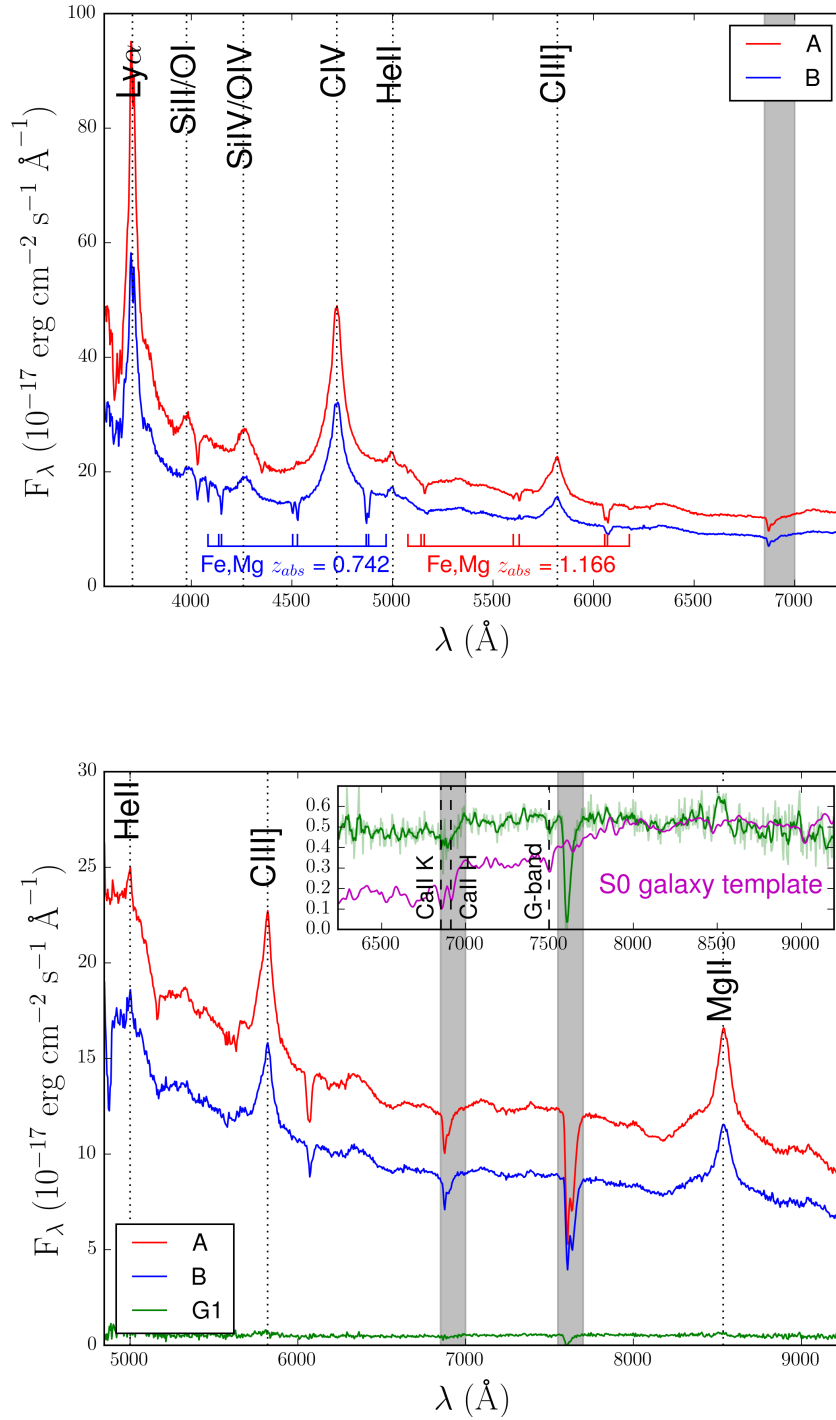**Table 2**.   GTC–OSIRIS–R500B spectra of SDSS J1515+1511AB.

λ^{a}	$F_\lambda(\mathrm{A})^{\mathrm{b}}$	$F_\lambda(\mathrm{B})^{\mathrm{b}}$
3567.142	48.233	32.704
3570.736	47.358	30.125
3574.330	48.826	29.310
3577.924	46.260	28.706
3581.518	48.972	32.073

[a] Observed wavelength in Å.

[b] Flux in 10^{-17} erg cm^{-2} s^{-1} Å^{-1}.

NOTE—Table 2 is published in its entirety in the machine-readable format. A portion is shown here for guidance regarding its form and content.

Figure 3. GTC–OSIRIS spectra of SDSS J1515+1511ABG1 in 2015. Vertical dotted lines indicate emission lines at $z_\mathrm{s} = 2.049$, while grey highlighted regions are associated with atmospheric artefacts. Top: R500B grism. The spectrum of B includes Fe I, Fe II, and Mg II absorption at $z_\mathrm{abs} = 0.742$, and the spectrum of A contains a notable Fe/Mg absorption at $z_\mathrm{abs} = 1.166$ (see Sections 4.2 and 5). Bottom: R500R grism. The top sub–panel displays a zoomed–in version of the G1 spectrum along with the red–shifted ($z = 0.742$) spectral template of an S0 galaxy (Kinney et al. 1996).

Table 3. GTC–OSIRIS–R500R spectra of SDSS J1515+1511ABG1.

λ^a	$F_\lambda(A)^b$	$F_\lambda(B)^b$	$F_\lambda(G1)^b$
4846.622	26.253	18.984	0.466
4851.437	23.692	16.945	0.551
4856.251	23.546	15.886	0.300
4861.066	23.258	14.193	0.598
4865.880	23.847	14.016	0.268

^{a}Observed wavelength in Å.

^{b}Flux in 10^{-17} erg cm^{-2} s^{-1} Å^{-1}.

NOTE—Table 3 is published in its entirety in the machine-readable format. A portion is shown here for guidance regarding its form and content.
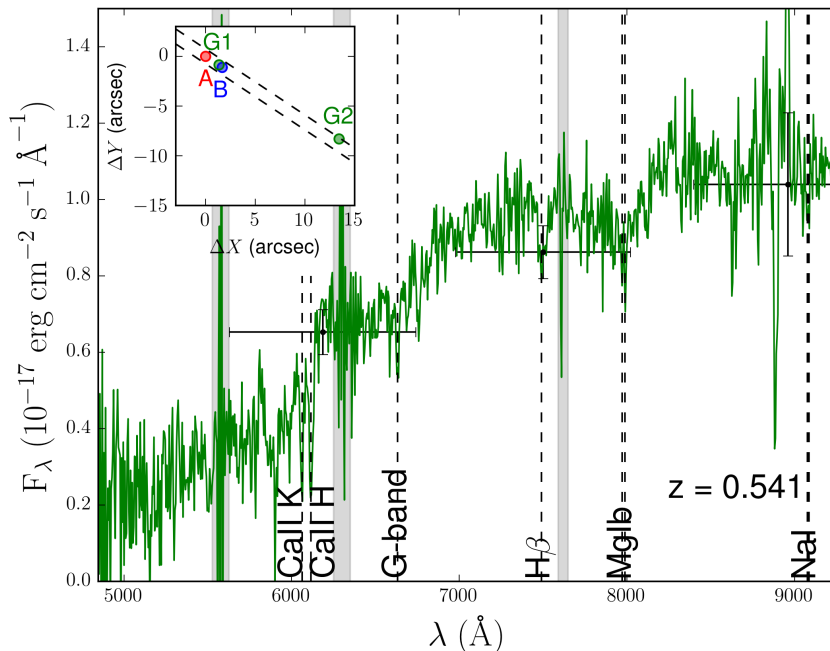
Figure 4. GTC–OSIRIS–R500R spectrum of the secondary galaxy G2. We also display several expected absorption features at $z_{G2} = 0.541$ (vertical dashed lines), and use crosses and grey rectangles to highlight the riz–SDSS fluxes and spectral regions associated with atmospheric artefacts, respectively. The observational configuration appears in the top sub–panel. This shows the four sources A, B, G1, and G2 within the slit edges (two parallel dashed lines).

To confirm or not the tentative redshift of the main lensing galaxy (0.742; Inada et al. 2014), we analysed the G1 spectrum in the top sub–panel inside the bottom panel of Figure 3. In spite of all our efforts with the GTC data, G1 appears as a very faint source with significant contamination by light of B. This contamination distorts its spectral shape by producing artefact peaks (e.g., Mg II residual flux at ∼8500 Å) and an almost flat continuum. Indeed, the spectrum of G1 does not display a noticeable drop off in flux at ∼7000 Å, which would correspond to a 4000 Å break in the rest frame of a disk–like galaxy without emission lines at a redshift of 0.742 (see the magenta line). Vertical dashed

lines indicate the positions of some expected absorption features at $z_{G1} = 0.742$, but unfortunately, these positions coincide with flux decrements that are indistinguishable from noise or are located in a sky absorption region. As a consequence, we were not successful in an unambiguous spectroscopic determination of z_{G1}. However, we were lucky because our GTC–OSIRIS–R500R long–slit exposures included light from the secondary galaxy G2 (see Section 1 and the top sub–panel inside Figure 4), and thus, we extracted the G2 spectrum and measured its redshift. Since G2 is $\sim 16''$ away from the A image, we used the IRAF/APEXRACT package to get an initial spectrum, and then the riz–SDSS magnitudes of the galaxy to peform an accurate flux calibration. The final spectrum is consistent with an early–type galaxy at $z_{G2} = 0.541$ (see Figure 4).

2.2.2. *Spectroscopic monitoring*

We are conducting a robotic monitoring of a small sample of $\sim$10 lensed quasars with images brighter than $r = 20$ mag and visible from the Northern Hemisphere (Goicoechea et al. 2015). Taking the spatial resolution of the LT spectrographs into account, we only consider spectroscopic monitoring campaigns of double quasars with image separation $\geq 2''$. For each such doubles, we obtain spectroscopic observations separated by the time delay between its two images, which allows us to study magnification ratios for the continuum and the emission lines at different wavelengths. These delay–corrected ratios (i.e., at the same emission time) are key tools to discuss the differential dust extinction, the macrolens magnification ratio, and microlensing effects in the system (e.g., Schneider et al. 2006).

We observed SDSS J1515+1511 with the SPRAT long–slit spectrograph on 2015 August 16. The $1''8$ ($\sim$4 pixel) wide slit was oriented along the line joining A and B, and we used the red grating mode. The grating may be set to two different configurations which are optimized for the blue or red regions of the $4000-8000$ Å wavelength range (resolving power of $\sim$350 at 6000 Å). This first night, we took 5×600 s exposures under normal observing conditions: FWHM $\sim 1''5$ at 6000 Å and airmass of $\sim$1.3. We also obtained 5×600 s LT–SPRAT–blue exposures on 2015 August 18 to check the best grating mode for this lens system. After getting the earliest SPRAT spectra in 2015 August, a second step was to decide on a sampling time based on some time delay estimation. While current lens models predict delays ranging from 5 to 7 months (Rusu et al. 2016), we used our two first photometric monitoring seasons (see Sections 2.1 and 3) to set the sampling time to 7 months. Thus, we have re–observed the system on 2016 March 17 to obtain 5×600 s LT–SPRAT–blue exposures under acceptable seeing conditions (FWHM $\sim 1''7$ at 6000 Å) with a low airmass of $\sim$1.05. We also observed the spectrophotometric standard star BD+33d2642 (Oke 1990) on each of the three monitoring nights in $2015-2016$.
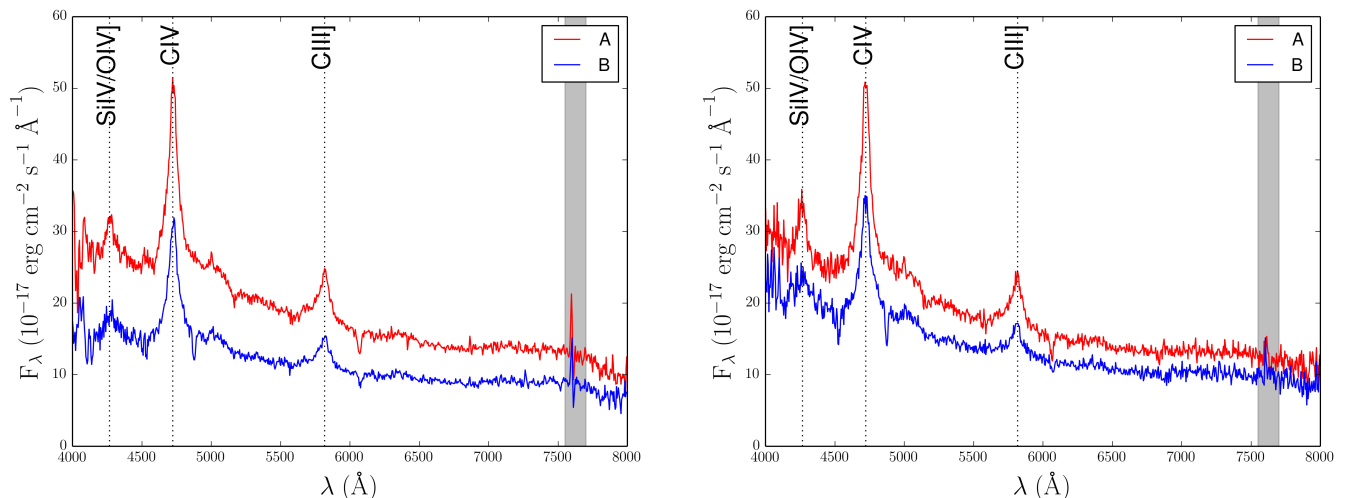
Figure 5. LT–SPRAT spectra of SDSS J1515+1511AB. Vertical dotted lines indicate emission lines at $z_s = 2.049$, while grey highlighted regions are associated with atmospheric artefacts. Left: 2015 August (total exposure time = 6 ks). Right: 2016 March (total exposure time = 3 ks).

The standard data reduction with IRAF included the same tasks that we used to process the GTC observations in Section 2.2.1. The spectra of the two quasar images were extracted by fitting two 1D Gaussian profiles with fixed separation. In a first iteration, the position of A, the width of the 1D PSF model, and the amplitudes of the two components were allowed to vary at each wavelength. In a second iteration, we only considered the multi–wavelength

instrumental fluxes of A and B as free parameters (see Section 2.2.1). From these instrumental spectra, the spectral response functions, and r–band fluxes from LT frames (taken on 2015 August 19 and 2016 March 18), we derived flux–calibrated spectra of A and B at the three observing epochs. The quasar spectra at the two first close epochs were then combined to make two spectral energy distributions (A and B) with lower noise (see the left panel of Figure 5). All final spectra are shown in Figure 5, and are also available in a tabular format (Tables 4 and 5). These contain Si IV+O IV], C IV, and C III] emission lines. It is also evident that the B spectrum varied appreciably on a timescale equal to the time delay of the lens system (see Section 3).

Table 4. LT–SPRAT–blue/red spectra of SDSS J1515+1511AB in 2015 August.

λ^{a}	$F_\lambda(\mathrm{A})^{\mathrm{b}}$	$F_\lambda(\mathrm{B})^{\mathrm{b}}$
3980.459	38.616	13.170
3985.095	37.200	16.612
3989.731	30.862	20.126
3994.368	32.590	18.687
3999.004	35.608	17.765

^{a}Observed wavelength in Å.

^{b}Flux in 10^{-17} erg cm^{-2} s^{-1} Å^{-1}.

Note—Table 4 is published in its entirety in the machine-readable format. A portion is shown here for guidance regarding its form and content.

**Table 5**. LT–SPRAT–blue spectra of SDSS J1515+1511AB in 2016 March.

λ^{a}	$F_\lambda(\mathrm{A})^{\mathrm{b}}$	$F_\lambda(\mathrm{B})^{\mathrm{b}}$
3968.467	25.244	24.423
3973.122	35.824	22.400
3977.776	40.208	24.188
3982.431	36.540	25.976
3987.086	34.417	26.696

^{a}Observed wavelength in Å.

^{b}Flux in 10^{-17} erg cm^{-2} s^{-1} Å^{-1}.

Note—Table 5 is published in its entirety in the machine-readable format. A portion is shown here for guidance regarding its form and content.

3. TIME DELAY

Assuming that the magnitude fluctuations in the right panel of Figure 1 mainly arise from intrinsic variations in the source quasar, we focused on two standard techniques to measure the time delay between A and B. First, we carried out a reduced chi–square (χ_r^2) minimization. This χ_r^2 minimization was based on a comparison between the light curve of A and the time–shifted light curve of B, using different lags and bins with semisize α in B (e.g., Ullán et al. 2006). For $\alpha \sim 10$ days, we found best solutions $\Delta t_{AB} \sim 210$ days ($\chi_r^2 \sim 1$), which are related with deep minima in χ_r^2–lag relationships (see the top panel of Figure 6). The uncertainties in Δt_{AB} and the r–band magnitude offset (Δr_{AB}) were derived from 1000 repetitions of the experiment (pairs of synthetic light curves based on the observed records). To obtain synthetic curves for A and B, we modified the observed magnitudes by adding random quantities. These random quantities were realizations of normal distributions around zero, with standard deviations equal to the measured errors. We obtained 5000 delays and magnitude offsets by applying the χ_r^2 minimization ($\alpha = 8, 9, 10, 11$ and 12 days) to the 1000 pairs of synthetic curves, and the corresponding distributions are shown in the bottom panels of Figure 6.
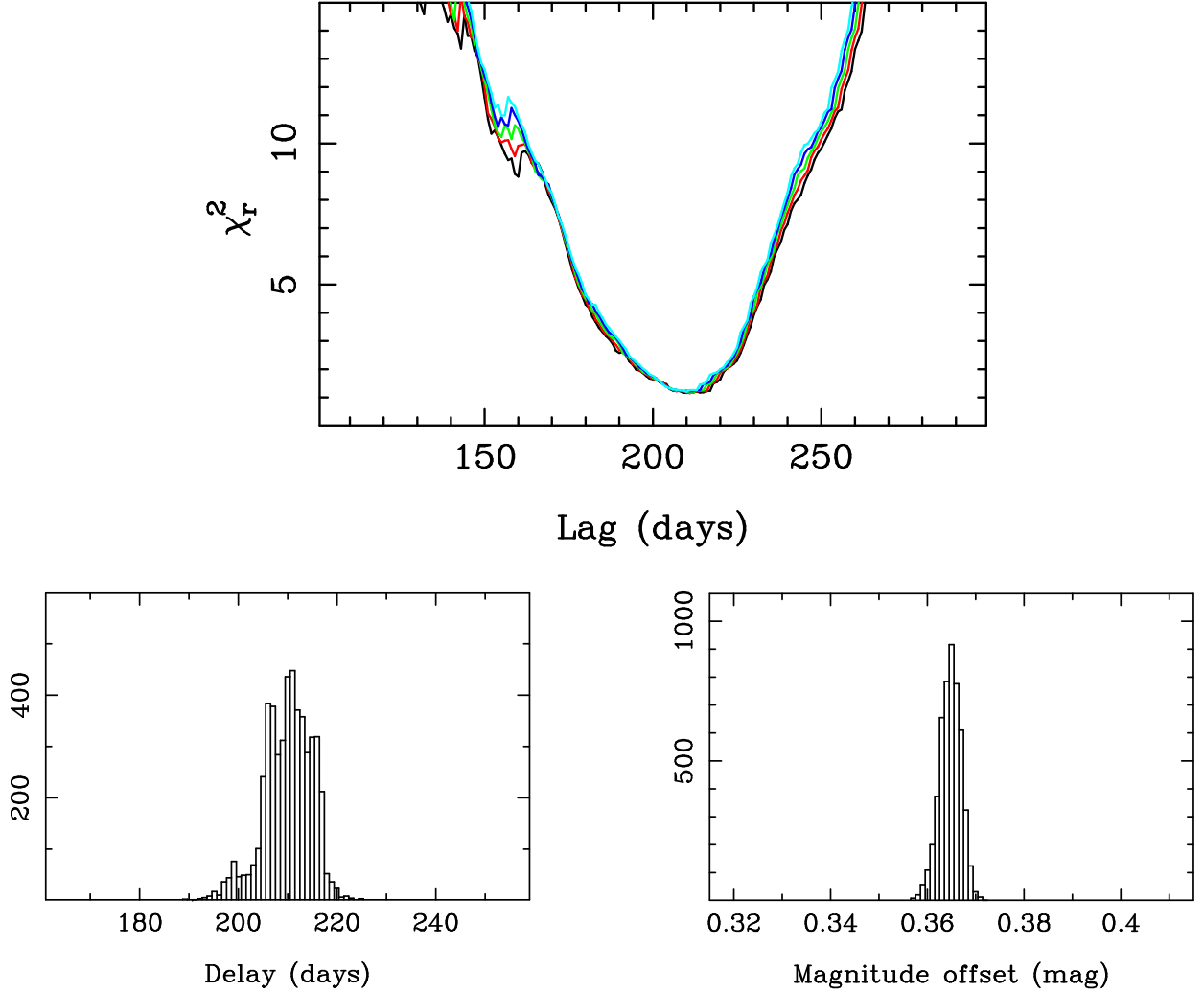
Figure 6. Top: χ_r^2–lag relationships for $\alpha = 8$ days (black), $\alpha = 9$ days (red), $\alpha = 10$ days (green), $\alpha = 11$ days (blue), and $\alpha = 12$ days (cyan). Bottom: Histograms from 1000 pairs of synthetic curves and the χ_r^2 minimization ($\alpha = 8-12$ days). The left and right panels display the best solutions of the time delay and the magnitude offset, respectively.

From the histograms in the bottom panels of Figure 6, we inferred the 1σ measurements (68% confidence intervals) in the first result row of Table 6. The time delay is 211^{+4}_{-5} days (A is leading), while the r–band magnitude offset (magnification ratio) is 0.3650 ± 0.0025 mag. We also used the dispersion minimization to estimate the delay and the offset. Thus, the $D_{4,2}^2$ estimator (Pelt et al. 1996) with decorrelation lengths $\delta = 8-12$ days produced a minimum at 211 days. Additionally, when applying the $D_{4,2}^2$ minimization ($\delta = 8-12$ days) to the 1000 pairs of synthetic curves,

we obtained the second result row of Table 6. Table 6 also provides composite measures ($\chi_{\mathrm{r}}^2 + D_{4,2}^2$) of the time delay and the magnitude offset, which have 2.4% and 0.7% accuracy, respectively.

Table 6. Time delay and magnitude offset in the r band of SDSS J1515+1511.

Method	Δt_{AB}	Δr_{AB}
χ_{r}^2	211_{-5}^{+4}	0.3650 ± 0.0025
$D_{4,2}^2$	211_{-4}^{+5}	0.3650 ± 0.0025
$\chi_{\mathrm{r}}^2 + D_{4,2}^2$	211 ± 5	0.3650 ± 0.0025

NOTE—Δt_{AB} in days and Δr_{AB} in magnitudes. A is leading, and all measurements are 68% confidence intervals.

From the central values in the time delay and magnitude offset intervals (211 days and 0.365 mag), we constructed the combined light curve in the r band (see Figure 7). Such combined curve consists of the B light curve (blue squares) and the magnitude– and time–shifted brightness record of A (red circles). Magnitude fluctuations in both quasar images agree well each other, indicating the absence of significant microlensing variability over the 2.6 years (three full seasons) of monitoring. This is in good agreement with our initial hypothesis in the beginning of this section. Despite the existence of sophisticated methods for determining time delays in presence of microlensing (e.g., Tewes et al. 2013), simpler standard techniques are enough here, and we adopt our composite measures as the final 1σ intervals.
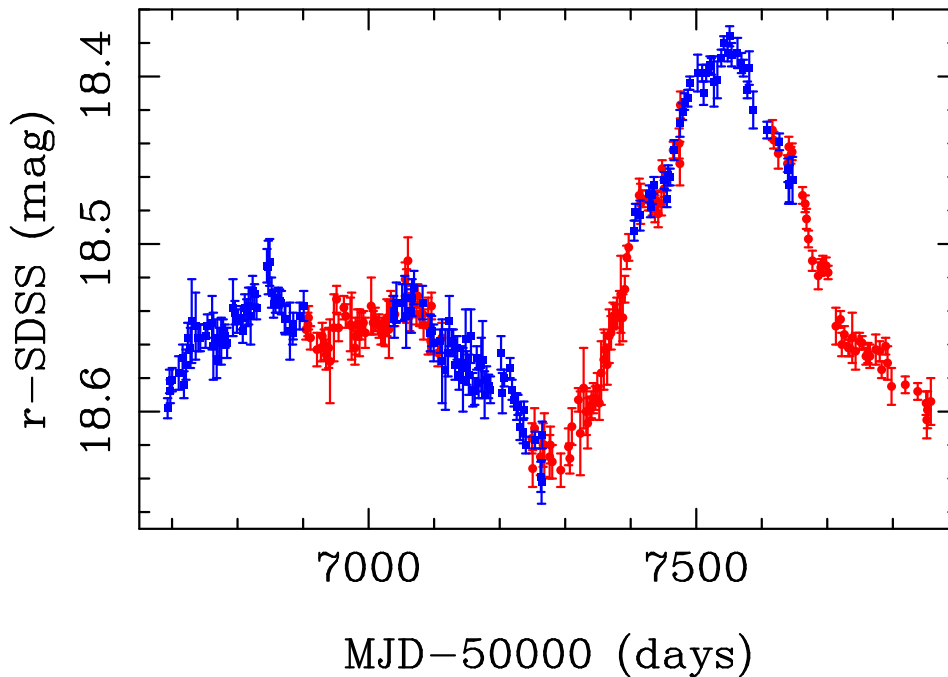
Figure 7. Combined light curve in the r band. The B curve (blue squares) and the magnitude– and time–shifted A curve (red circles) are drawn together (see main text).

The Δt_{AB} interval in the last result row of Table 6 is marginally consistent with the delay interval for the SIE+γ lens model in Table 5 of Rusu et al. (2016). Hence, the constraints used in that paper seem to be close to the actual ones. In Section 4, assuming the tentative redshift $z_{\mathrm{G1}} = 0.742$ (see Section 1), we discuss the macrolens magnification ratio from the GTC and LT spectroscopic data. This is compared with the K'–band magnitude difference $B - A$ (at the same observing time) in the Rusu et al.'s paper. In Section 5, the new constraints on the macrolens magnification

ratio and the time delay are used to check the current SIE+γ lens model and to validate the assumed redshift of G1 (e.g., Goicoechea & Shalyapin 2010).

4. DUST EXTINCTION, MACROLENS MAGNIFICATION AND MICROLENSING EFFECT

4.1. *Analysis of the main emission lines*

The GTC–OSIRIS spectra of SDSS J1515+1511AB include five main emission lines: Lyα, Si IV/O IV], C IV, C III], and Mg II, three of which are also present in the LT–SPRAT spectra of the quasar images (see Figures 3 and 5). After de–redshifting these spectra to their rest frame (using z_s = 2.049), we analysed the features of interest. The GTC–OSIRIS–R500B data show prominent Lyα, Si IV/O IV], C IV, and C III] emissions in each image, and the corresponding line profiles were obtained in a standard way. We took two continuum windows for each emission feature (one on its left side and the other on its right), fitted a linear function to the data in both windows, and then removed the continuum level in the spectral region.

In a second step, we performed a multi–component decomposition of these continuum–subtracted line profiles. Such a decomposition has been previously used in many spectral studies (e.g., Wills et al. 1985; Kuraszkiewicz et al. 2002; Dietrich et al. 2003; Sluse et al. 2007; Marziani et al. 2010). For each emission line, its two profiles (A and B data) were modelled as a sum of Gaussian components, i.e., primary components of the line plus other secondary contributions blended with primary ones. In a first stage, we only decomposed the A profile by fitting the central wavelength of primary components (a single Gaussian or two Gaussians with different widths; by setting the wavelength separations between primary and secondary components to known values), as well as the widths and amplitudes of all components. For the B profile having lower signal strength, the central wavelength of primary components and the widths of all contributions were taken from the output of the first stage. Thus, in a second stage, we fitted the B data leaving only the amplitudes as free parameters.

To reproduce the Lyα profiles, we used a single primary (Lyα) component plus a red–wing excess due to N V, while we considered a single component to describe the Si IV/O IV] profiles (see the top panels of Figure 8). The C IV line shapes were well traced by two primary contributions (narrow and broad) plus a He II complex. This complex is a blend of several lines, and was treated as a secondary Gaussian component (e.g., Croom et al. 2002). Regarding the C III] profiles, we used two C III] components (narrow and broad), as well as two blue–wing excesses caused by Si III] and Al III (e.g., Brotherton et al. 1994). The carbon line profiles and their decompositions are shown in the middle panels of Figure 8. The GTC–OSIRIS–R500R spectra include the Mg II emission line, which is not present in the blue grism data. Hence, we also carried out the analysis of the Mg II emission in each image. We extracted the two continuum–subtracted profiles in a standard way (see above), and then did decompositions into a single Gaussian component (see the bottom panel of Figure 8). To avoid the wings of the Mg II line that are presumably contaminated by Fe II/Balmer emission (e.g., Wills et al. 1985), we exclusively fitted the 40 Å width central region.

Although we do not detect variations of the Si IV/O IV], C IV, C III], and Mg II emissions in the A image (in Figure 8, there is great similarity between the GTC–OSIRIS profiles and the SDSS/BOSS line shapes observed three years before), the LT–SPRAT spectra allow us to directly compare A and B profiles at the same emission time. These spectra were taken at two epochs separated by the time delay between images (see Sections 2.2.2 and 3), so we compared the A profiles on 2015 August 16−18 with the B profiles on 2016 March 17. The LT–SPRAT data do not cover the Mg II emission, and their Si IV/O IV] signals were too noisy to be useful. We thus concentrated on the carbon line profiles (see Figure 9), which were obtained and decomposed as those in Figure 8. From the right panel of Figure 9, we see that the C III] decomposition for the B image is far from robust.

From the profiles and decompositions in Figures 8 and 9, it is straightforward to obtain magnitude differences for emission line cores and components. For a given emission line (in the GTC–OSIRIS or LT–SPRAT spectra), $(B-A)_{\rm core} = -2.5\log(B/A)_{\rm core}$ was estimated by integrating the A and B profiles over a 20 Å width central region (line core), while $(B-A)_{\rm comp} = -2.5\log(B/A)_{\rm comp}$ for each of its components was derived by integrating the two associated Gaussian distributions. In addition, the 1σ confidence intervals for the magnitude differences were determined from 1000 pairs AB of simulated spectra in the region of interest. We obtained a pair AB of simulated spectra in the same manner as a pair of synthetic light curves in Section 3. Instead of photometric errors, here we used the standard deviations of the residual flux in the two continuum windows to add random deviations to the observed fluxes. In Table 7, we present our measurements of $(B-A)_{\rm core}$ and $(B-A)_{\rm comp}$ having relative errors less than 10%. We note that all line components have widths exceeding the instrumental ones of $\sim 2-3$ Å.
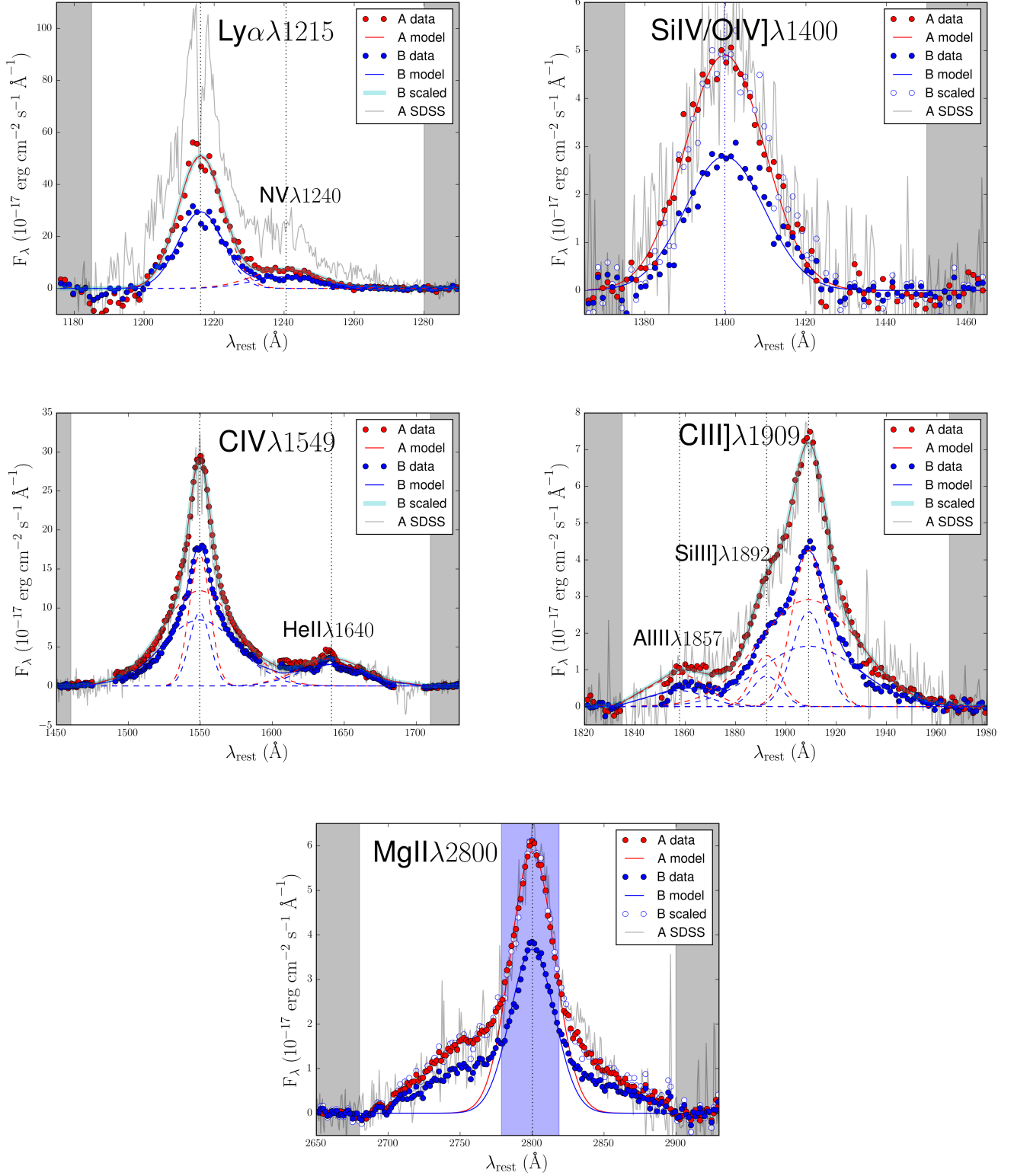
Figure 8. Line profiles and multi–component decompositions from the GTC–OSIRIS data of A and B. The top and middle panels display the results for the Lyα, Si IV/O IV], C IV, and C III] emission lines in the blue grism spectra, whereas the bottom panel shows the results for the Mg II emission in the red grism spectra. The profiles for the A image on 2015 April 15−16 (red circles) are compared with profiles from the SDSS/BOSS spectrum of A on 2012 April 13 (grey lines). We also highlight the continuum windows (grey rectangles), as well as the 40 Å width central region of the Mg II line (blue rectangle in the bottom panel). See main text for details.
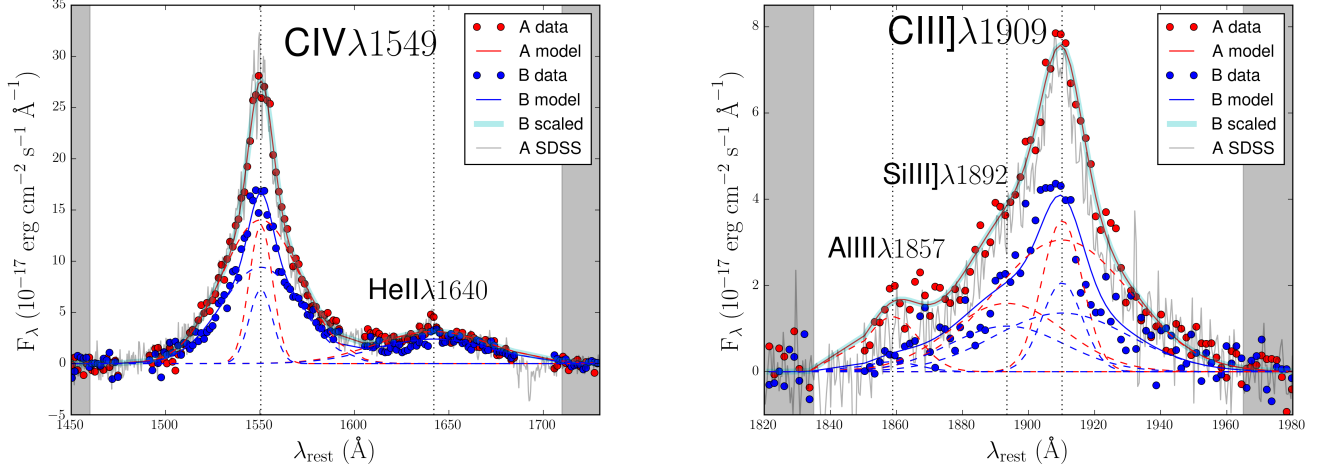
Figure 9. Line profiles and multi–component decompositions from the LT–SPRAT data of A and B. We compare the A profiles/decompositions on 2015 August 16−18 with the B profiles/decompositions on 2016 March 17. We also show the continuum windows used to extract the line shapes (grey rectangles) and the A profiles from SDSS/BOSS data on 2012 April 13 (grey lines). See main text for details.

Table 7. Analysis of emission lines.

Instrument	Main line	$\lambda_{\rm rest}$[a] (Å)	$(B-A)_{\rm core}$[b] (mag)	Component	$\sigma_{\rm comp}$[c] (Å)	$(B-A)_{\rm comp}$[b] (mag)
GTC–OSIRIS–R500B	Lyα	1216.09 ± 0.15	0.590 ± 0.030	single	6.37 ± 0.16	0.595 ± 0.028
	Si IV+O IV]	1399.83 ± 0.16	0.628 ± 0.037	single	9.88 ± 0.17	0.614 ± 0.038
	C IV	1549.58 ± 0.02	0.512 ± 0.003	narrow	7.25 ± 0.09	0.629 ± 0.008
				broad	26.16 ± 0.33	0.398 ± 0.008
				He II	22.89 ± 0.36	0.345 ± 0.022
	C III]	1909.61 ± 0.37	0.584 ± 0.013	narrow	6.15 ± 0.87	0.544 ± 0.038
				broad	19.37 ± 2.72	0.608 ± 0.053
GTC–OSIRIS–R500R	Mg II	2800.25 ± 0.10	0.509 ± 0.010	single	15.32 ± 0.15	0.507 ± 0.010
LT–SPRAT	C IV	1550.43 ± 0.13	0.507 ± 0.017	narrow	6.17 ± 0.34	0.681 ± 0.063
	C III]	1910.38 ± 1.16	0.643 ± 0.057	$\cdots$	$\cdots$	$\cdots$

[a] Central wavelength of primary components of the line in the rest frame of the source ($z_{\rm s} = 2.049$)

[b] Magnitude difference at the same observing time (GTC–OSIRIS) or at the same emission time (i.e., magnification ratio; LT–SPRAT). $(B-A)_{\rm core}$ is estimated in the 20 Å wide core (rest frame) of the primary emission, while $(B-A)_{\rm comp}$ is associated with a primary component (single, narrow or broad) or a secondary one

[c] Rest-frame standard width of the Gaussian component

4.2. *Solutions for the visual extinction and macrolens magnification ratios*

Although the ideal procedure to obtain a reliable extinction–macrolens solution for SDSS J1515+1511 is to use pure narrow lines arising from the NLR (e.g., Moustakas & Metcalf 2003), there are no available data on this type of emission lines. Thus, in this section, the magnitude differences in Table 7 are used to study the visual extinction and macrolens magnification ratios in the lens system. The line cores are presumably produced in extended regions that are unaffected by microlensing (e.g., Motta et al. 2012, and references therein), and this hypothesis is assumed true unless evidence indicates otherwise. We focused on the five lines in the GTC–OSIRIS spectra, i.e., magnitude differences at the same observing time, checking through previous SDSS/BOSS data of A and the LT–SPRAT results

for the carbon lines whether intrinsic variability is playing a role.

For the Lyα and Si IV/O IV] lines, their $(B - A)_{\mathrm{core}}$ values are close to and consistent with the magnitude differences for their single primary components (see the two first result rows of Table 7). We taken the line–core differences as the two first data to get extinction–macrolens solutions. For the GTC–OSIRIS C IV emission line, we have a richer information, and detect a $B - A$ gradient: $(B - A)_{\mathrm{narrow}} \sim 0.63$, $(B - A)_{\mathrm{core}} \sim 0.51$, and $(B - A)_{\mathrm{broad}} \sim 0.40$. In this case, even the line core seems to be affected by microlensing, and we considered the $(B - A)_{\mathrm{narrow}}$ value as the third data point for our study of extinction–macrolens parameters. We remark that the existence of microlensing in the C IV line core is also supported by the results derived from the LT–SPRAT spectra. For the other carbon line (C III]) in the GTC–OSIRIS spectra, the $(B - A)_{\mathrm{narrow}}$ and $(B - A)_{\mathrm{broad}}$ values have large uncertainties, so they are consistent with each other and with the line–core difference. We taken this last difference (fourth data point) because it has the smallest error. For the Mg II line, we considered its $(B - A)_{\mathrm{core}}$ value (fifth data point), which basically coincides with the difference for the single primary component.
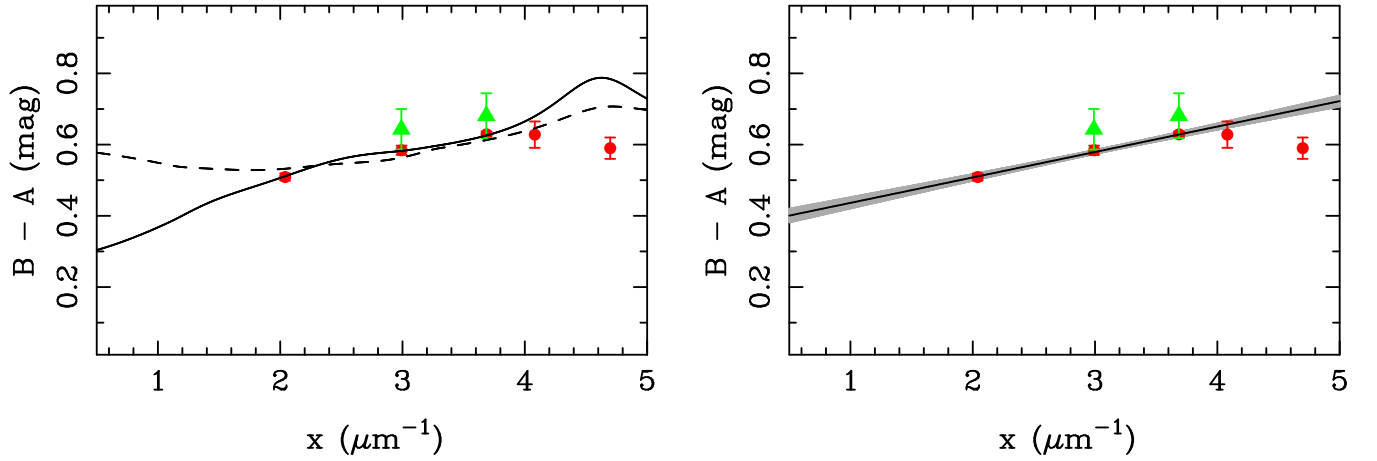
Figure 10. Extinction curve for SDSS J1515+1511. We display seven magnitude differences (see main text): five GTC–OSIRIS data for the Lyα, Si IV/O IV], C IV, C III], and Mg II emission lines (red circles), and two LT–SPRAT data for the carbon lines (green triangles). The x–axis represents the inverse of the wavelength in the rest frame of G1. Left: Assuming a Galactic extinction law in G1, the dashed and solid lines describe the best fits using all the GTC–OSIRIS data and the first four GTC–OSIRIS differences (excluding the data point for the Lyα emission), respectively. Right: Assuming a linear extinction law in G1, we show the best fit to the first four GTC–OSIRIS differences (solid line) and its 1σ band (light grey area).

First, we fitted a Galactic extinction model to the five GTC–OSIRIS magnitude differences that are described in the previous paragraph. The model was relied on the general formalism for the differential extinction in a pair of lensed images (e.g., Falco et al. 1999; Wucknitz et al. 2003; Elíasdóttir et al. 2006), assuming the presence of Milky Way–like dust (Cardelli et al. 1989) in the main lensing galaxy at $z_{\mathrm{G1}} = 0.742$. More specifically, we used the equation (2) of Shalyapin & Goicoechea (2014) to obtain a best fit with $\chi^2 \sim 27$ (two degrees of freedom). This poor model fit is largely due to the large residual for the Lyα magnitude difference (see the dashed line in the left panel of Figure 10). As shown in Figure 8, despite the similarity between the Si IV/O IV], C IV, C III], and Mg II line profiles from the GTC–OSIRIS and SDSS/BOSS data of the A image, the Lyα line strength from the GTC–OSIRIS data of A is substantially smaller than that derived through previous SDSS/BOSS observations of the same image (three years before). Therefore, there is evidence of Lyα variability in the A image, and this precludes the use of the GTC–OSIRIS Lyα magnitude difference in the fits. When fitting the model to exclusively the differences at $x = (1 + z_{\mathrm{G1}})/\lambda \sim 2$–4 $\mu\mathrm{m}^{-1}$, i.e., excluding the Lyα measurement, we found a best fit with $\chi^2 \sim 2$ (one degree of freedom; see the solid line in the left panel of Figure 10).

In spite of the notable improvement in the reduced chi–square value when we do not take the Lyα difference into account, the Galactic extinction model does not work satisfactorily because $\chi_r^2 \sim 2$ is still large. Thus, we also fitted a linear extinction model to the GTC–OSIRIS Si IV/O IV], C IV, C III], and Mg II differences. The linear extinction law describes reasonably well the dust effects at $x \sim 2$–4 $\mu\mathrm{m}^{-1}$ (e.g., Prévot et al. 1984), and we used the equation (3) of Shalyapin & Goicoechea (2014) with $\alpha = 1$. This standard linear model fits much better than the Galactic model, since we obtained $\chi^2 \sim 1$ with two degrees of freedom. In the right panel of Figure 10, we present the best fit (solid line) and the 1σ band (light grey area). As expected, the Lyα difference (last red circle) behaves as an outlier, while there is an acceptable agreement between the carbon differences at the same observing time (GTC–OSIRIS) and the

same emission time (LT–SPRAT). The macrolens magnification and visual extinction ratios are $\Delta m_{AB} = 0.365 \pm 0.023$ and $\Delta A_{AB}(V) = 0.130 \pm 0.013$ mag, respectively (1σ intervals).

It is noteworthy that our 68% confidence interval for Δm_{AB} incorporates central values of the wider range used by Rusu et al. (2016) to infer their SIE+γ lens model. To account for time delay, dust extinction, and microlensing effects (e.g., Yonehara et al. 2008), they considered the K'–band magnitude difference with an increased error (0.34 $\pm$ 0.11 mag) as a proxy to Δm_{AB}. Furthermore, we are implicitly assuming that the strong absorber at $z_{abs} = 0.742$ (intervening gas) reported by Inada et al. (2014) is associated with intervening dust at the same redshift. The new GTC spectrum of the B image in the top panel of Figure 3 also shows this Fe/Mg absorption system, which is not detected in the GTC spectrum of the A image. We consistently find that the B image is more affected by dust extinction, i.e., $A_B(V) > A_A(V)$.

4.3. Evidence for quiescent microlensing activity

In Figure 11, we show the four GTC–OSIRIS magnitude differences (filled red circles) that have been used to obtain the best extinction–macrolens solution (solid line). In addition, the light grey rectangle below these circles highlights the 1σ confidence interval for the macrolens magnification ratio. For the C IV emission line, we have reported on a $B - A$ gradient in Section 4.2. This supports the presence of microlensing in the C IV BLR, since $B - A$ decreases from ~ 0.63 (GTC–OSIRIS narrow component that is originated in a very extended region; third filled red circle in Figure 11) to ~ 0.40 (GTC–OSIRIS broad component arising from a relatively compact BLR; open red circle under the third filled red circle), passing through an intermediate value of ~ 0.51 (GTC–OSIRIS and LT–SPRAT line–core differences; filled red and open green squares). Regarding the He II (broad) component in the GTC–OSIRIS spectra, its $(B - A)$ value is slightly less than $(B - A)_{broad}$ for the C IV emission (see the two open red circles), which is an additional evidence for microlensing in the high–ionisation BLR (e.g., Guerras et al. 2013, and references therein).
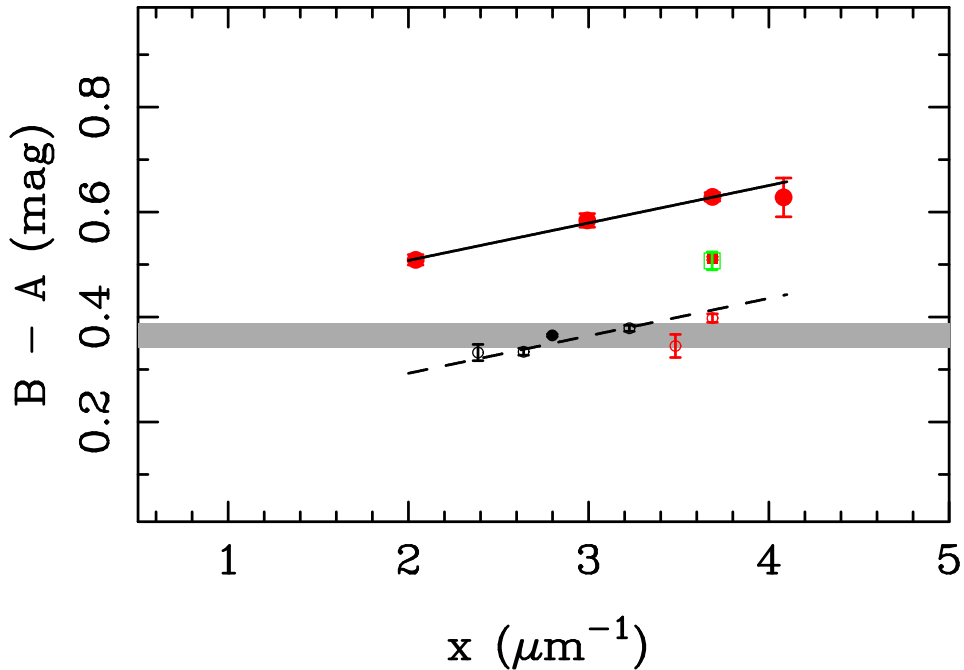
Figure 11. Magnification ratios in SDSS J1515+1511. The four filled red circles represent the GTC–OSIRIS magnitude differences for the C IV narrow component, and the Si IV/O IV], C III], and Mg II line cores. As reference, the best fit in the right panel of Figure 10 is also drawn (solid line). For the C IV emission line, the filled red and open green squares represent the GTC–OSIRIS and LT–SPRAT line–core differences, respectively. We also show the GTC–OSIRIS differences for the C IV and He II broad components (open red circles). These two differences and four additional LT ratios for the continuum (black circles; see main text) are distributed around a straight line (dashed line) parallel to the best extinction–macrolens solution (solid line). The light grey rectangle describes the 1σ confidence interval for the macrolens magnification ratio.

In Figure 11, we also display LT magnification ratios for the continuum at different wavelengths: the filled black circle represents our 1σ measurement of Δr_{AB} in Section 3, while the three open black circles represent 1σ measurements from LT–SPRAT data in three 200 Å wide spectral intervals centred at 5400, 6600, and 7300 Å. These black circles suggest that the continuum emitting region (accretion disk) and the high–ionisation BLR suffer a similar microlensing

effect of ~ 0.2 mag (the dashed line serves as a guide to the eye). Our observations in both the wavelength and time domains indicate that the compact sources are crossing microlensing magnification regions without appreciable gradients.

5. LENSING MASS DISTRIBUTION

Rusu et al. (2016) used the relative astrometry of SDSS J1515+1511ABG1 and the magnitude difference $B - A$ (see Table 3 of that paper), as well as the observed ellipticity and orientation of G1 (see Table 4 of that paper), to obtain a SIE+γ lens model. These observational constraints were inferred from high–resolution K'–band imaging on 2012 February 21, and the mass of G1 was reasonably modelled as a SIE that is aligned with the observed light distribution. Within such a framework, the SIE has only one free parameter (Einstein radius $\theta_{\rm Ein}$), and the galaxies outside the strong lensing region produce an external shear that is characterised by two additional free parameters: shear strength (γ) and direction (θ_γ). Because the number of model parameters was the same as the number of observational constraints, Rusu et al. obtained a perfect fit with $\chi^2 \sim 0$.

While the Rusu et al.'s results for the lensing mass parameters were derived through the GLAFIC software (Oguri 2010), we used the LENSMODEL software (Keeton 2001) to analyse the lens system. Although different software packages may lead to different output results for the same lens scenario (e.g., Lefor & Futamase 2015), we reproduced the Rusu et al.'s GLAFIC best–solution for the SIE+γ scenario by using the LENSMODEL package (see the second column of Table 8). The GLAFIC and LENSMODEL definitions of $\theta_{\rm Ein}$ for a SIE differ by a factor $f(q) = [(1 + q^2)/2q]^{1/2}$, where $q = b/a = 1 - e$ is the axis ratio and e is the ellipticity. Thus, in Table 8, we quote the values of $\theta_{\rm Ein}({\rm GLAFIC}) = \theta_{\rm Ein}({\rm LENSMODEL}) \times f(q)$. Instead of the Rusu et al.'s constraint on $\Delta m_{\rm AB}$ (or equivalently, on the macrolens flux ratio B/A), we considered the new accurate measurement in Section 4.2. Moreover, we also incorporated the measured time delay (Section 3) as an additional constraint. This allowed us to fit the redshift of the lensing mass z_l by assuming a concordance cosmology with $H_0 = 70$ km s^{-1} Mpc^{-1}, $\Omega_m = 0.27$, and $\Omega_\Lambda = 0.73$ (Komatsu et al. 2009). Regarding the source redshift, we taken $z_{\rm s} = 2.049$ rather than 2.054 (see discussion in Section 1).

Table 8. SIE+γ mass model.

Parameter	Rusu et al. (2016)	This paper
$\theta_{\rm Ein}$	$1''\!.21$	$1''\!.21$
e	(0.81)	(0.81)
θ_e	$(-17^\circ\!.1)$	$(-17^\circ\!.1)$
γ	0.283	0.286
θ_γ	$76^\circ\!.0$	$76^\circ\!.0$
z_l	$\cdots$	0.729
χ^2	~ 0	~ 0

NOTE—Here, $\theta_{\rm Ein}$, e, γ, and z_l denote Einstein radius, ellipticity, external shear strength, and lens redshift, respectively; and position angles (θ_e and θ_γ) are measured east of north. The quantities within parentheses were not fitted, but fixed at values derived from the light distribution of G1.

Our best values of $\theta_{\rm Ein}$, γ, and θ_γ (see the third column of Table 8) just about match those of the Rusu et al. Concerning the lens redshift, its best value is slightly lower than 0.742, which has been used to obtain the constraint on the macrolens magnification ratio in Section 4.2. However, the formal 1σ interval (0.729 ± 0.011 for $\Delta\chi^2 \leq 1$) is consistent with $z_l \sim 0.74$, and the best value of z_l should be increased in presence of an external convergence (see discussion at the end of this section). Additionally, a moderately high value of $H_0 = 72$ km s^{-1} Mpc^{-1} (studies of Cepheids, maser galaxies, supernovae, gravitational lenses, and other astrophysical objects support $H_0 \sim 72 - 74$ km s^{-1} Mpc^{-1}; e.g., Freedman & Madore 2010; Jackson 2015) led to $z_l = 0.742$. Despite our failure in accurately solving

the G1 spectrum and to measure its redshift directly, it is easy to reconcile the lens redshift with the assumed redshift of G1. This last result strongly supports that G1 is located at $z_{\rm G1} = 0.742$.

We remark that dark matter halos of some galaxies other than G1 could extend to the strong lensing region, so the SIE+γ scenario could be not so realistic as it seems. Apart from the absorber most likely associated with G1, the top panel of Figure 3 displays a more distant Fe/Mg absorption system ($z_{\rm abs} = 1.166$) that is seen in both quasar images, but affecting A in a more significant manner. The secondary galaxy G2 may also play a role. For instance, taking into account $z_{\rm G2} = 0.541$, as well as the angular separation between this galaxy and the quasar images $\theta \sim 15''$, we found that the dark matter halo of G2 may reach the region of interest at ~ 100 kpc. Therefore, using a singular isothermal sphere (SIS) to describe the mass of G2, we studied the possible gravitational effect at the position of the double quasar. Assuming that $K(\rm G2) \sim K'(\rm G2) = 17.4$ mag (Rusu et al. 2016), the lensing Faber–Jackson relation (Rusin et al. 2003) yielded a dark matter velocity dispersion $\sigma_{\rm DM}(\rm G2) \sim 196$ km s^{-1}. If $z_{\rm l}$ were equal to $z_{\rm G2}$, the SIS would produce a convergence and shear of $\kappa = \gamma \sim 0.023$ at $\theta \sim 15''$. However, as G2 lies at a redshift different to $z_{\rm l}$, the effective convergence and shear would be $\kappa_{\rm eff} = \gamma_{\rm eff} \sim 0.015$ (Momcheva et al. 2006). Thus, G2 may account for only a small fraction of the external shear in Table 8, while it could be responsible of a slight increase in $z_{\rm l}$ (see discussion in Goicoechea & Shalyapin 2010).

6. SUMMARY AND CONCLUSIONS

This analysis uses new LT light curves (and spectra) and GTC spectra of the gravitational lens system SDSS J1515+1511 to measure the time delay between its two quasar images (A and B), as well as to discuss effects and physical properties of intervening objects. All optical data correspond to observations over the last 3 years. Our main results and conclusions are (error bars represent 1σ confidence intervals):

1) We find that the lensed quasar lacks microlensing activity. This means that the accretion disk and the inner BLR are suffering an almost constant differential magnification by microlenses (stars) in the main lensing galaxy G1.

2) The intrinsic fluctuations seen in the r–band LT light curves of A and B (with an amplitude of ~ 0.1–0.3 mag) lead to a robust time delay $\Delta t_{\rm AB} = 211 \pm 5$ days (A is leading). In the current quiescent state of microlensing activity, SDSS J1515+1511 is particularly well suited for reverberation mapping studies. After detecting a prominent event in an optical light curve of A, one has several months to prepare a multiwavelength monitoring of B (e.g., Gil-Merino et al. 2012; Dahle et al. 2015).

3) Our GTC data do not allow us to extract an accurate spectrum of G1, which is fainter than 22 mag in the r band. However, Fe/Mg absorption features in the GTC–OSIRIS–R500B spectrum of the quasar image closer to G1 (B image) suggest that $z_{\rm G1} = 0.742$ (see the top panel of Figure 3 and earlier findings by Inada et al. 2014). Assuming this redshift for G1, we carefully analyse the differential extinction in G1 and the macrolens magnification ratio $\Delta m_{\rm AB}$. From the main emission lines in the GTC spectra of the quasar (with the help of LT and SDSS/BOSS spectra), we infer a visual extinction ratio of 0.130 ± 0.013 mag (B is redder), in agreement with the presence of more dust where there is more gas. In addition, we obtain $\Delta m_{\rm AB} = 0.365 \pm 0.023$ mag.

4) We use previous observational constraints on the relative astrometry of the lens system and the morphology of G1 (Rusu et al. 2016), together with the new constraints on the time delay and the macrolens magnification ratio, to update the Rusu et al.'s SIE+γ lens model. Our results for the mass scale of the SIE (G1) and the external shear practically coincide with those of Rusu et al., and using a standard concordance cosmology, we derive an 1σ interval for the lens redshift $z_{\rm l}$ that is marginally consistent with the assumed redshift of G1. Additionally, there is some evidence for the existence of a small external convergence (see below) leading to a better agreement between $z_{\rm l}$ and $z_{\rm G1}$. We also obtain $z_{\rm l} = 0.742$ for $H_0 = 72$ km s^{-1} Mpc^{-1} (e.g., Freedman & Madore 2010; Jackson 2015). Thus, our mass modelling confirms the tentative value of $z_{\rm G1}$ in the discovery paper (Inada et al. 2014).

5) It should be noted that a SIE+γ lens scenario is not the only possible. Both quasar images intercept a Fe/Mg absorption system at a redshift of 1.166, which may play a role. We also measure the redshift of the secondary galaxy G2, which is nearer than G1 and has a dark matter velocity dispersion of about 200 km s^{-1} (SIS model; using the scheme of Rusin et al. 2003). If the mass distribution in G2 would extend up to ~ 100 kpc, then it would produce $\sim 5\%$ of the external shear and an external convergence of ~ 0.015.

Facilities: Liverpool:2m(IO:O and SPRAT), GTC(OSIRIS)

Software: IRAF, IMFITFITS, LENSMODEL

REFERENCES

Abajas, C., Mediavilla, E., Muñoz, J. A., Popović, L. Č., & Oscoz, A. 2002, ApJ, 576, 640

Brotherton, M. S., Wills, B. J., Steidel, C. C., & Sargent, W. L. W. 1994, ApJ, 423, 131

Cardelli, J. A., Clayton, G. C., & Mathis, J. S. 1989, ApJ, 345, 245

Croom, S. M., Rhook, K., Corbett, E. A., et al. 2002, MNRAS, 337, 275

Dahle, H., Gladders, M. D., Sharon, K., Bayliss, M. B., & Rigby, J. R. 2015, ApJ, 813, 67

Dietrich, M., Hamann, F., Appenzeller, I., & Vestergaard, M. 2003, ApJ, 596, 817

Elíasdóttir, Á., Hjorth, J., Toft, S., Burud, I., & Paraficz, D. 2006, ApJS, 166, 443

Eulaers, E., Tewes, M., Magain, P., et al. 2013, A&A, 553, 121

Falco, E. E., Impey, C. D., Kochanek, C. S., et al. 1999, ApJ, 523, 617

Fassnacht, C. D., & Cohen, J. G. 1998, AJ, 115, 377

Freedman, W. L., & Madore, B. F. 2010, ARA&A, 48, 673

Gil-Merino, R., Goicoechea, L. J., Shalyapin, V. N., & Braga, V. F. 2012, ApJ, 744, 47

Goicoechea, L. J., & Shalyapin, V. N. 2010, ApJ, 708, 995

Goicoechea, L. J., & Shalyapin, V. N. 2016, A&A, in press [eprint arXiv:1609.07440]

Goicoechea, L. J., Shalyapin, V. N., & Gil-Merino, R. 2015, eprint arXiv:1505.04317

Guerras, E., Mediavilla, E., Jiménez-Vicente, J., et al. 2013, ApJ, 764, 160

Hainline, L. J., Morgan, C. W., MacLeod, C. L., et al. 2013, ApJ, 774, 69

Howell, S. B. 2006, Handbook of CCD Astronomy (Cambridge, Cambridge Univ. Press)

Inada, N., Oguri, M., Rusu, C. E., Kayo, I., & Morokuma, T. 2014, AJ, 147, 153

Jackson, N. 2015, Living Rev. Relat., 18, 2

Jahnke, K., Wisotzki, L., Courbin, F., & Letawe, G. 2007, MNRAS, 378, 23

Keeton, C. R. 2001, eprint arXiv:astro-ph/0102340

Kinney, A. L., Calzetti, D., Bohlin, R. C., et al. 1996, ApJ, 467, 38

Komatsu, E., Dunkley, J., Nolta, M. R., et al. 2009, ApJS, 180, 330

Kundić, T., Turner, E. L., Colley, W. N., et al. 1997, ApJ, 482, 75

Kuraszkiewicz, J. K., Green, P. J., Forster, K., et al. 2002, ApJS, 143, 257

Lefor, A. T., & Futamase, T. 2015, eprint arXiv:1505.00502

Marziani, P., Sulentic, J. W., Negrete, C. A., et al. 2010, MNRAS, 409, 1033

McLeod, B. A., Bernstein, G. M., Rieke, M. J., & Weedman, D. W. 1998, AJ, 115, 1377

Møller, P. 2000, The Messenger, 99, 31

Momcheva, I., Williams, K., Keeton, C., & Zabludoff, A. 2006, ApJ, 641, 169

Morgan, C. W., Eyler, M. E., Kochanek, C. S., et al. 2008, ApJ, 676, 80

Mosquera, A. M., & Kochanek, C. S. 2011, ApJ, 738, 96

Motta, V., Mediavilla, E., Falco, E., & Muñoz, J. A. 2012, ApJ, 755, 82

Moustakas, L. A., & Metcalf, R. B. 2003, MNRAS, 339, 607

Ofek, E. O., & Maoz, D. 2003, ApJ, 594, 101

Ofek, E. O., Maoz, D., Rix, H. W., Kochanek, C. S., & Falco, E. E. 2006, ApJ, 641, 70

Oguri, M. 2010, PASJ, 62, 1017

Oke, J. B. 1974, ApJS, 27, 21

Oke, J. B. 1990, AJ, 99, 1621

Pelt, J., Kayser, R., Refsdal, S., & Schramm, T. 1996, A&A, 305, 97

Prévot, M. L., Lequeux, J., Maurice, E., Prévot, L., & Rocca-Volmerange, B. 1984, A&A, 132, 389

Rathna Kumar, S., Tewes, M., Stalin, C. S., et al. 2015, A&A, 557, 44

Refsdal, S. 1964, MNRAS, 128, 307

Refsdal, S. 1966, MNRAS, 132, 101

Richards, G. T., Keeton, C. R., Pindor, B., et al. 2004, ApJ, 610, 679

Rojas, K., Motta, V., Mediavilla, E., et al. 2014, ApJ, 797, 61

Rusin, D., Kochanek, C. S., Falco, E. E., et al. 2003, ApJ, 587, 143

Rusu, C. E., Oguri, M., Minowa, Y., et al. 2016, MNRAS, 458, 2

Schneider, P., & Wambsganss, J. 1990, A&A, 237, 42

Schneider, P., Kochanek, C. S., & Wambsganss, J. 2006, Gravitational Lensing: Strong, Weak & Micro, Proc. of the 33rd Saas-Fee Advanced Course, ed. G. Meylan, P. Jetzer, & P. North (Berlin, Springer)

Shalyapin, V. N., & Goicoechea, L. J. 2014, A&A, 568, 116

Shalyapin, V. N., Goicoechea, L.J., Koptelova, E., Ullán, A., & Gil-Merino, R. 2008, A&A, 492, 401

Sluse, D., Claeskens, J. F., Hutsemékers, D., & Surdej, J. 2007, A&A, 468, 885

Tewes, M., Courbin, F., & Meylan, G. 2013, A&A, 553, 120

Udalski, A., Szymański, M. K., Kubiak, M., et al. 2006, Acta Astron., 56, 293

Ullán, A., Goicoechea, L. J., Zheleznyak, A. P., et al. 2006, A&A, 452, 25

Wills, B. J., Netzer, H., & Wills, D. 1985, ApJ, 288, 94

Wucknitz, O., Wisotzki, L., López, S., & Gregg, M. D. 2003, A&A, 405, 445

Yonehara, A., Hirashita, H., & Richter, P. 2008, A&A, 478, 95